

# Cooling Mixed A-Site Halide Perovskites: Impact of Temperature on Optical and Structural Properties

Colette M. Sullivan,<sup>▽</sup> Jason E. Kuszynski,<sup>▽</sup> Alexey Kovalev, Nozomi Shirato, Volker Rose, Sarah Wieghold, Theo Siegrist, Richard D. Schaller, Geoffrey F. Strouse, and Lea Nienhaus\*



Cite This: *Chem. Mater.* 2024, 36, 9874–9881



Read Online

ACCESS |



Metrics & More

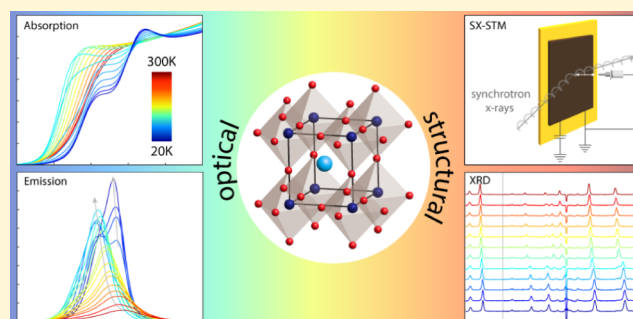


Article Recommendations



Supporting Information

**ABSTRACT:** The widespread utilization of perovskite-based photovoltaics requires probing both the structural and optical properties under extreme operating conditions to gain a holistic understanding of the material behavior under stressors. Here, we investigate the temperature-dependent behavior of mixed A-site cation lead triiodide perovskite thin films (85% methylammonium and 15% formamidinium) in the range from 300 to 20 K. Through a combination of optical and structural techniques, we find that the tetragonal-to-orthorhombic phase transition occurs at  $\sim 110$  K for this perovskite composition, as indicated by the change in the diffraction pattern. With decreasing temperature, the quantum yield increases with a concurrent elongation of the carrier lifetimes, indicating suppression of nonradiative recombination pathways. Interestingly, in contrast to single A-site cation perovskites, an additional optical transition appears in the absorption spectrum when the phase transition is approached, which is also reflected in the emission spectrum. We propose that the splitting of the optical absorption and emission is due to local segregation of the mixed cation perovskite during the phase transition.



## INTRODUCTION

Lead halide perovskites have experienced an explosive increase in research efforts largely due to their impressive power conversion efficiencies, which now rival those of silicon solar cells.<sup>1</sup> This is almost entirely due to their promising (opto)electronic properties, which include long carrier lifetimes and diffusion lengths,<sup>2–4</sup> simple compositional band gap tunability,<sup>5–7</sup> and a high absorption cross section in the visible and near-infrared spectral region.<sup>8</sup> Despite their fundamental promise to act as the active layer in photovoltaics (PVs)<sup>4,9–11</sup> or light-emitting diodes (LEDs),<sup>12–14</sup> one of their major drawbacks is insufficient long-term stability particularly under operating conditions of elevated temperatures and continuous illumination.<sup>15–17</sup> Mitigation strategies to improve stability at elevated temperatures include compositional engineering: by generating mixed cation and mixed halide compositions, the Goldschmidt tolerance can be tuned, a critical factor to increase the perovskite stability.<sup>18</sup>

However, considering that perovskite PVs can easily be fabricated on flexible, lightweight substrates,<sup>19,20</sup> perovskite PVs can find use as transportable devices for use in remote regions of the world, including at low temperature conditions, such as high elevation or arctic regions, or considered as viable solar panels for use in space travel where they would be exposed to temperature extremes both high and low.<sup>21–23</sup> While the effect of multiple stressors on the performance of

perovskite-based devices, such as elevated temperatures, applied electric fields, and continuous illumination, has been receiving increased interest, the effects of low temperatures are not yet sufficiently understood and will provide important insight into the overall performance of the devices.

Several key factors make the low temperature studies particularly interesting: (i) The lead halide perovskites that are used in PV or LED applications exhibit low exciton binding energies, which can be overcome with ambient thermal energy to produce free carriers rather than excitons.<sup>24</sup> (ii) A first order phase transition occurs at  $\sim 110$  K for this composition, corresponding to the transition from the tetragonal to the orthorhombic phase.<sup>25</sup> In addition to the phase transition, lattice contractions are observed, which decrease the average distance between the ions and influence electron–phonon coupling as the phase transition temperature is approached.<sup>26</sup>

In this work, we investigate the impact of temperature changes on the optical bandgap, the crystal structure, and the recombination dynamics after excitation for a mixed cation

Received: July 19, 2024

Revised: August 20, 2024

Accepted: September 4, 2024

Published: September 26, 2024



perovskite thin film comprised of 85% methylammonium (MA), 15% formamidinium (FA) lead triiodide ( $\text{MA}_{0.85}\text{FA}_{0.15}\text{PbI}_3$ , MAFA).<sup>25</sup> In contrast to previous low temperature studies on  $\text{MAPbI}_3$ , which shows the splitting of the emission into the orthorhombic phase and one additional low energy emission feature below the phase transition temperature,<sup>27</sup> our results indicate that the emission splits into three distinct emissive features for the mixed cation lead halide perovskite investigated here.

## MATERIALS AND METHODS

**Film Fabrication.** Glass substrates were cleaned by 15 min of sonication in the following solutions: 2% Hellmanex, deionized water, ethanol, and acetone, and then placed in a UV–ozone plasma cleaner (Ossila) for an additional 15 min. Precursor solutions of 1.2 M methylammonium iodide (MAI, Dyenamo) and formamidinium iodide (FAI, Dyenamo) were prepared in a DMF/DMSO (9:1 v/v, Sigma) containing lead iodide. These solutions were diluted to either half or one-fifth of the original concentration in order to make the  $\sim 100$  and  $\sim 30$  nm films, respectively. The precursor solutions were deposited onto the substrates and spin coated using a two-step program: 1000 rpm for 10 s and 5000 rpm for 30 s. Chlorobenzene (Sigma) was used as the antisolvent, and the thin films were annealed at 100 °C for 15 min. All films were encapsulated in an inert nitrogen-filled glovebox using a two-part epoxy (Devcon). For the temperature-dependent XRD studies, films were deposited onto sapphire substrates in an effort to minimize the background. Samples for the SX-STM investigations were deposited onto ITO substrates to ensure sufficient conductivity within the STM.

**Steady-State Optical Spectroscopy.** All visible absorption spectra were collected by using a Thermo Scientific Evolution 220 spectrophotometer.

Steady-state PL spectra were collected by an Ocean Optics spectrometer (HR2000 + ES). Emission for all films were collected under a 405 nm continuous wave laser (LDH-D-C-405, PicoQuant) at 0.6 mW. Excess laser scatter was removed via a 425 nm long-pass filter (Chroma Tech.).

**Time-Resolved Photoluminescence Spectroscopy.** Time-resolved PL measurements for the perovskite PL decays were collected under 405 nm picosecond pulsed excitation (LDH-D-C-405, PicoQuant) at 200 kHz and 0.2  $\mu\text{W}$ . A 425 nm long-pass filter (Chroma Technology) was used to isolate the perovskite PL and minimize laser scattering. The single photon counting avalanche photodiode used was from Micro Photon Devices, and all collected PL decays were histogrammed with a HydraHarp 400 (PicoQuant) event timer.

**Temperature Control.** Temperature control for steady-state and time-resolved emission studies were achieved by a He-filled cryocooler (Air Products). Encapsulated films were mounted onto a coldfinger optical sample mount prior to sheath evacuation ( $\sim 10^{-5}$  mBar) where a PID Digital Temperature Controller Model 9650 (Scientific Instruments) was used to maintain the desired temperature. For each temperature point, the coldfinger was left to equilibrate for approximately 1 min prior to collecting spectra.

**Transient Absorption Spectroscopy.** Transient absorption was performed using an 800 nm, 35 fs pulse width, 2 kHz, amplified titanium:sapphire laser (Spectra Physics, Spitfire). White light probe pulses were produced by focusing a portion of the output into a 2 mm thick sapphire crystal following a time delay that was controlled by using a mechanical delay stage and retroreflector. Pump pulses were produced using an optical parametric amplifier (Light Conversion, TOPAS) that afforded tunable near-infrared light, which was then converted into red photons via harmonic generation. The pump was reduced to a 1 kHz repetition rate using a mechanical chopper. Both the pump and probe were focused and overlapped on the sample with the pump spot exceeding twice the diameter of the probe. Probe pulses were spectrally dispersed after passing through the sample and compared for pump-on versus pump-off intensity on a single shot

basis. All data was collected under a 650 nm pump at 0.6 mW (179  $\mu\text{m}$  spot size).

**X-ray Diffraction.** The XRD diffraction experiments were performed using a Rigaku UltraX-18 rotating anode generator with a Cu source. The X-ray radiation from the source passed through an elliptic mirror, specifically designed for the Cu  $K\alpha$  wavelength (AXO Dresden GmbH,  $f_1 = 350$  mm,  $f_2 = 3500$  mm), to increase the signal intensity. The reflections were measured using a hybrid pixel area detector (DECTRIS Pilatus 300k wide) with the pixel size of  $0.172 \times 0.172$  mm<sup>2</sup>. The distance from the sample to the detector was about 430 mm along the normal plane of the detector. The sample was placed under vacuum and mounted on a copper sample holder inside a Displex 201 closed-cycle cryocooler with Be walls for X-ray transparency. During the measurements, the sample orientation with respect to the incoming beam was determined by optimizing the observed reflection.

**SX-STM (XAS).** Temperature-dependent SX-STM experiments were performed at the XTIP beamline at sector 4-ID-E of the Advanced Photon Source and Center for Nanoscale Materials at Argonne National Laboratory. Each measurement was operated in an ultrahigh vacuum environment ( $< 5 \times 10^{-10}$  Torr) where a special metal–insulator–metal “smart tip” was used made of tungsten wire<sup>28</sup> placed  $\sim 1$   $\mu\text{m}$  above the sample. The photon energy was ramped between 610 and 680 eV with a step size of 0.2 eV at a resolving power  $E/dE$  of 4000.<sup>29</sup> Temperature control was achieved by using a flow cryostat operated with liquid nitrogen.

## RESULTS AND DISCUSSION

The absorption and the emission properties of the MAFA perovskite are monitored between 300 and 20 K in steps of 10 K (Figure 1a,b). In agreement with our previous results on the perovskite properties in MAFA/rubrene bilayer upconversion

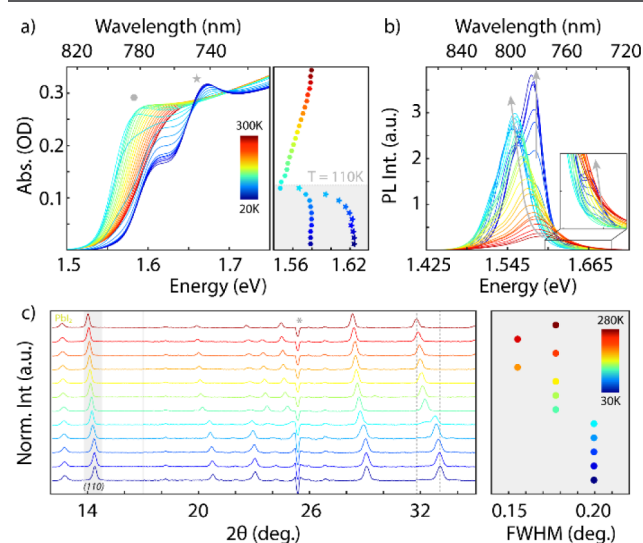


**Figure 1.** (a) (left) Temperature-dependent absorbance spectra of MAFA (100 nm) cooling from 300 to 20 K (red to blue) taken every 10 K. (right) Bandgap energies for the main features observed in the absorbance spectra indicated by octagons and stars. (b) MAFA PL taken under 405 nm excitation while cooling from 300 to 20 K measured every 10 K. Spectral inset highlights the growth of the feature at 754 nm. Gray arrows highlighting peak shifts are included to aid the eye. (c) (left) Temperature-dependent XRD of MAFA cooling from 280 to 30 K taken every 10 K. For ease of comparison, the patterns were normalized to the (110) reflection for  $2\theta < 15^\circ$  and (220) reflection for  $2\theta > 15^\circ$ . Dotted gray lines are included as guides to the eye to highlight the perovskite reflection shift. (right) FWHM of the (110) MAFA reflection across the different temperatures. The asterisk denotes a detector artifact.

devices,<sup>25</sup> a redshift in both the absorption onset and the steady-state photoluminescence (PL) are observed when the temperature is decreased. Between 110 and 100 K, the absorption onset rapidly blue shifts and splits into two distinct optical transitions. This initial redshift with decreasing temperature followed by a discrete jump in the optical bandgap has been previously investigated for methylammonium lead iodide (MAPbI<sub>3</sub>) perovskites (Figure S1) and can be traced back to a first-order phase transition from the tetragonal to the orthorhombic perovskite phase.<sup>27</sup> In agreement with previous reports,<sup>30,31</sup> the decrease in bandgap with decreasing temperature is at odds with the expected Varshni-type behavior of most semiconductors. The unusual bandgap renormalization in lead halide perovskites is caused by their electronic structure: the conduction band minimum is generated by the hybridization of the Pb 6*p* orbital and the 5*p* orbital of I and has *p*-like character. The valence band maximum is created by the antibonding orbital obtained from the hybridization of the Pb 6*s* and I 5*p* orbitals. Since the bandgap is dictated by the Pb and I orbitals, the bandgap will be influenced by the thermal expansion of the I–Pb–I bonds but are dominated by electron–phonon interactions in the [PbI<sub>6</sub>]<sup>−</sup> octahedra.<sup>30,32</sup> We find slight hysteresis of the optical properties (compare Figures S2 and S3), which is in agreement with a first-order phase transition and indicates that the transition temperature shifts slightly based on the direction of the temperature change.

To ensure that the splitting of the absorption onset for the mixed cation perovskite investigated here is not simply due to an incomplete phase transition, the impact of the temperature on the crystal structure was investigated by using X-ray diffraction (XRD). In agreement with previous results for MAPbI<sub>3</sub>, the reflections for MAFA continuously shift to larger angles up to the phase transition, indicating a lattice contraction with decreasing temperature (Figure 1c). A first order phase transition is observed at ~110 K, as indicated by the splitting and sudden shift of reflections at angles 2θ = 19.9 and 31.8° corresponding to the (112) and (130) reflections of the tetragonal phase at 280 K.<sup>33</sup> Following the phase transition, reflections corresponding to a different (orthorhombic) crystal structure are observed below the temperature of 110 K (Figure 1c). Since XRD indicates a single perovskite crystal structure, without additional impurity reflections present, the splitting of the optical transition seen in the low temperature absorption is unlikely caused by an incomplete phase transition.

A closer look at the PL spectra at 20 K reveals the emergence of an emission shoulder at 754 nm, in addition to the two main PL peaks at 784 and 796 nm. Previously, the observation of dual emission in the single cation perovskite MAPbI<sub>3</sub> has been attributed to several possibilities namely: (i) free exciton and bound exciton emission,<sup>34,35</sup> (ii) a donor–acceptor pair and free exciton emission,<sup>36</sup> (iii) tetragonal inclusions in the orthorhombic crystal structure,<sup>37–39</sup> and (iv) molecular disorder of the A-site cation in the orthorhombic crystal phase.<sup>27</sup> To account for the additional optical transition observed within the absorption spectrum in MAFA, as well as the three distinct emission peaks, we introduce an additional possibility: the local variation of the mixed cation composition. Here, we propose that the splitting of the optical absorption and emission is due to the local segregation of the mixed cation perovskite during the phase transition. As a result, a methylammonium-richer (MA<sub>0.85+x</sub>FA<sub>0.15−x</sub>PbI<sub>3</sub>) phase and a formamidinium-richer (MA<sub>0.85−x</sub>FA<sub>0.15+x</sub>PbI<sub>3</sub>) phase is ob-

tained which have slightly different bandgap energies. Cation migration requires a diffusive regime,<sup>40</sup> i.e., A-site vacancies, which are expected in the nonstoichiometric MAFA used here. As the PbI<sub>6</sub> octahedra tilt during the phase transition,<sup>40–42</sup> we suggest that the A-site cations migrate to form locally stable structures—laying a foundation for the formation of the methylammonium-richer (MA<sub>0.85+x</sub>FA<sub>0.15−x</sub>PbI<sub>3</sub>) phase and formamidinium-richer (MA<sub>0.85−x</sub>FA<sub>0.15+x</sub>PbI<sub>3</sub>) phases. Due to the minor differences in the resulting *d*-spacing of the crystal structures of MA<sub>0.85</sub>FA<sub>0.15</sub>PbI<sub>3</sub> and FA<sub>0.85</sub>MA<sub>0.15</sub>PbI<sub>3</sub>,<sup>43</sup> minor changes in between the two composition crystal structures are not expected to noticeably shift the reflections. Rather a broadening in reflection is expected due to increases in both local strain and disorder as well as a superposition of the reflections for the different compositions (Figure 1c, right).

Taking a deeper look into the distinct PL features in the temperature range from 300 K (λ = 776 nm) to 20 K (λ = 797, 792, and 756 nm), we find a continuous redshift of the perovskite PL peak position with decreasing temperature until the phase transition is reached, in agreement with current literature reports.<sup>27,36,39,44</sup>

We find that each PL spectrum is best fit by a linear combination of three Gaussian functions until 70 K is reached, after which four Gaussian functions are required to fully capture the spectral shape (Figures 2a and S4). For consistency

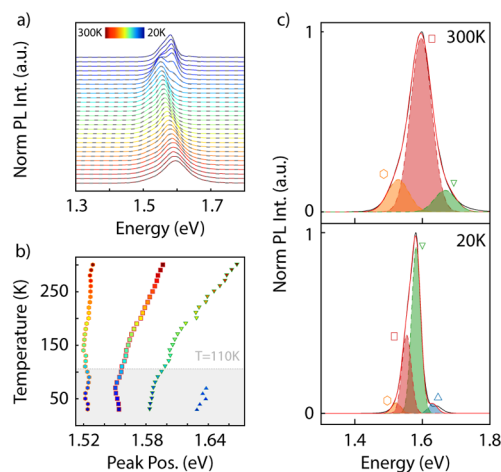


**Figure 2.** (a) Normalized temperature-dependent MAFA PL collected under 405 nm excitation cooling from 300 to 20 K measured every 10 K. Gray dashed lines are the sum of the multi-Gaussian fits for each temperature. (b) Peak energy of the MAFA emission extracted from the Gaussian fits as a function of temperature. The light gray box denotes the phase transition at 110 K. (c) Representative MAFA spectra at 300 K (top) and 20 K (bottom) showing the peak energy of the individual components of the Gaussian fits.

across the temperature scan, the full-width half-maximum (FWHM) for all peaks at a given temperature point are fixed; however, the amplitude and peak position are allowed to float. We attribute the individual Gaussians to the tetragonal mixed MA/FA perovskite emission, excitonic emission, and the orthorhombic phase emission.<sup>27,36</sup> As performed previously for inorganic semiconductors and lead halide perovskites,<sup>45,46</sup> useful photophysical properties are extracted by fitting the FWHM of the temperature dependent PL spectra via a Fröhlich Hamiltonian described in eq 1:

$$\Gamma(T) = \Gamma_0 + \gamma_{LO}/[e^{(E_{LO}/k_B T)} - 1] \quad (1)$$

Here,  $\Gamma_0$  is the temperature-independent inhomogeneous broadening,  $\gamma_{LO}$  is the charge carrier longitudinal optical (LO) phonon coupling strength,  $E_{LO}$  is energy of the LO-phonon, and  $k_B$  is Boltzmann's constant (Figure 3). Assuming negligible

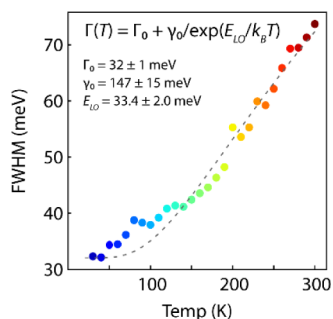


**Figure 3.** FWHM of the MAFA (100 nm) temperature-dependent PL emission with the corresponding fit (dashed gray line) of the included equation.

ionized impurity scattering, the fitting results in parameters  $\Gamma_0 = 32$  meV,  $\gamma_{LO} = 60$ , and  $E_{LO} = 23.3$  meV.  $\Gamma_0$  and  $\gamma_{LO}$  are comparable to MAPbI<sub>3</sub> and MAPbBr<sub>3</sub> results obtained previously, correlating to a higher MA content MAFA perovskite.<sup>46</sup> Additionally, a slight increase in FWHM relative to the fit is observed for between 50–140 K (close to or below the phase transition), which is consistent with defect-related PL appearing in the low temperature regime for MAPbI<sub>3</sub> and MAPbBr<sub>3</sub>;<sup>46</sup> however, fitting with a shared FWHM across the energy spectrum may reduce the observed impact from defect emission. The  $E_{LO}$  is higher than reported for FAPbBr<sub>3</sub> and FAPbI<sub>3</sub>,<sup>46</sup> consistent with a MA-dominant MAFA mixed-cation perovskite.

Figure 4 shows the temperature-dependent PL decay dynamics of MAFA measured at selected temperatures. Each

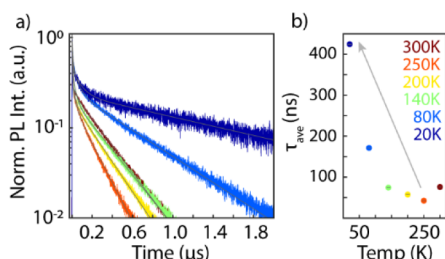


**Figure 4.** (a) Temperature-dependent MAFA (100 nm) lifetimes taken under 405 nm excitation at 200 kHz. Corresponding triexponential fits are included as gray traces. (b) Amplitude-weighted average lifetimes,  $\tau_{ave}$ , for the 405 nm lifetimes.

decay is best fit with a triexponential function (eq 2) due to multiple recombination pathways, including trap-assisted monomolecular recombination, excitonic or free carrier recombination, and Auger-assisted recombination processes.<sup>24,47</sup>

$$t = A_1 \cdot \exp\left(-\frac{t}{\tau_1}\right) + A_2 \cdot \exp\left(-\frac{t}{\tau_2}\right) + A_3 \cdot \exp\left(-\frac{t}{\tau_3}\right) \quad (2)$$

The calculated amplitude-weighted average lifetimes  $\tau_{ave} = \sum A_i \tau_i / \sum A_i$  for each decay are plotted in Figure 4b and shown in Table 1. Here we find the expected general trend: the

**Table 1.** Fitting Parameters for the Temperature-Dependent MAFA Lifetimes Based on a Triexponential Fit

Temp (K)	$A_1$	$\tau_1$ (ns)	$A_2$	$\tau_2$ (ns)	$A_3$	$\tau_3$ (ns)	$\tau_{ave}$ (ns)
300	0.63	1.83	0.071	31.0	0.25	293	79.7
250	0.68	2.74	0.12	35.9	0.18	201	43.4
200	0.65	3.99	0.16	26.4	0.19	261	57.4
140	0.55	5.51	0.26	29.5	0.20	312	74.0
80	0.44	8.51	0.26	54.7	0.26	599	179
20	0.52	6.37	0.22	80.5	0.24	1703	435

carrier lifetimes increase with decreasing temperatures. Lowering the temperature is expected to have a clear impact on the carrier dynamics, as the reduced ambient energy will increase the energetic barrier for carriers to escape even shallow traps, making trapping times longer. As a result, the observed PL decay will appear to be longer lived.

Initially, there is a decrease to  $\tau_{ave}$  upon cooling from 300 to 250 K, which we attribute to an initial rearrangement in the perovskite crystal structure when lowering the temperature due to the fact that it is not observed upon increasing the temperature back to 300 K (Figure S5). This can be explained by local regions of the perovskite structure still being “locked” in the cubic structure formed during annealing despite after the tetragonal structure being favored at room temperature, i.e., an effect based on the hysteresis observed in the perovskite phase transitions.

An additional early time rapid decay component becomes apparent at temperatures below 140 K. Multiple possible explanations are possible, namely: (i) a decrease in the dielectric constant with decreasing temperature caused by the rotation of the [PbI<sub>6</sub>]<sup>−</sup> octahedra during the tetragonal → orthorhombic phase transition and a shift of the Pb–I–Pb bond angle away from 180°, which in turn reduces the shielding of defects. (ii) Increased excitonic emission due to a reduction in ambient thermal energy, reducing the number of free carriers generated, and (iii) the possibility of rapid charge transfer between the different emissive states<sup>27</sup> or rapid trapping of excitons or charge carriers in shallow trap sites such as surface defects.

Probing further into the underlying temperature-dependent effects in the perovskite, we utilize synchrotron X-ray scanning tunneling microscopy (SX-STM) to ensure that the observed changes in the crystal structure and recombination dynamics are not due to degradation that could result in different chemical environments for the iodine ions and facilitate changes in the recombination dynamics.<sup>48</sup> Figure 5a shows the instrumental schematic for the SX-STM studies. Here, the STM tip is held  $\sim 1$   $\mu\text{m}$  away (far-field mode) from the surface of the sample, where monochromatic soft X-rays illuminate the tip–sample junction. Photoejected electrons are then collected either via the tip where they subsequently generate an additional current detected by the STM, or by monitoring the sample current caused by the total number of ejected electrons, yielding the total electron yield (TEY).<sup>49–51</sup> Hence, we can collect X-ray absorption (XAS) spectra by monitoring the TEY from the sample as a function of the photon energy. Utilizing soft X-rays, we are able to probe the  $3d_{3/2}$  ( $M_4$ ) and  $3d_{5/2}$  ( $M_5$ ) transitions for iodine. We can gain insight into the

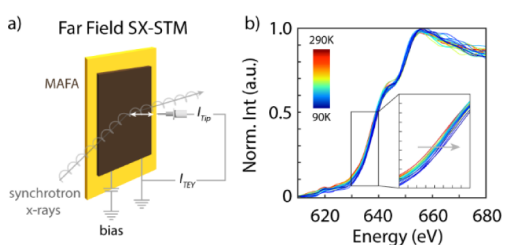


**Figure 5.** (a) Schematic for the temperature-dependent SX-STM measurements. (b) SX-STM of the  $I M_{4,5}$  edge for MAFA (30 nm). Each trace is the average of the spectra for every 10 K interval. Inset highlights the shifting rising edge as the temperature decreases. All spectra were taken in the far field under no applied bias of  $V = 0$ .

XAS spectrum for the cubic-to-tetragonal-to-orthorhombic phase transitions across this wide temperature range by looking at the iodine  $I M_{4,5}$  rising edge at  $\sim 645$  eV. Figure 5b shows the XAS spectra for the 30 nm MAFA thin films from 290 to 90 K. As the temperature decreases, no strong variations in the  $I M_{4,5}$  XAS spectra are observed, indicating that despite clear changes in the long-range crystal structure, the short-range chemical environment of the iodine ions is not significantly impacted during the phase transitions. A slight shift of the absorption onset to higher energies is observed as the temperature is decreased (compare inset Figure 5b), which can be attributed to the lattice contraction observed with decreasing temperature: shortening of the Pb–I bond will lead to an increase in the observed core energy levels, and hence an increase in the energy of the XAS onset.<sup>52</sup>

Lastly, ultrafast transient absorption (TA) measurements are performed to examine the influence of temperature on the charge carrier behavior. The characteristic perovskite dual photobleaching (PB2 and ground state bleach, GSB) and photoinduced absorption (PIA) features are seen across all measured temperatures (Figure 6a). As expected, the GSB narrows with decreasing temperature. The origin of the high

energy bleach PB2 is thought to stem from either a dual valence band structure<sup>3</sup> or a molecular charge–transfer complex.<sup>53</sup> Interestingly, at the two temperatures straddling the transition temperature at 110 K (140 and 80 K), we observe a splitting in the GSB at later delay times, as well as a drastic change to the spectral shape to the perovskite PIA. This is likely due to a similar effect as observed (*vide supra*) in the PL—separation of the cations into FA- and MA-rich local domains. Here, the splitting causes an additional high energy bleach feature to appear at 484 nm at 80 K thus decreasing the PIA and altering the spectral shape of the broad PIA.

Comparison of the GSB kinetics shows a decrease in the bleach recovery lifetime with decreasing temperature (Figure 6b,c). These kinetics are best fit with a multiexponential decay (triexponential until 140 K, then biexponential at 80 K). Again, comparison of the average weighted lifetime  $\tau_{ave}$  shows a decrease with decreasing temperature (Table 2). Figure 6d

**Table 2.** Fitting Parameters for the MAFA GSB Kinetics Based on a Multiexponential Fitting and the Amplitude-Weighted Average Lifetime  $\tau_{ave}$

Temp (K)	$A_1$	$\tau_1$ (ps)	$A_2$	$\tau_2$ (ps)	$A_3$	$\tau_3$ (ns)	$\tau_{ave}$ (ps)
298	0.42	10.53	0.36	242	0.34	4130	1340
250	0.56	9.92	0.29	223	0.30	2960	817
200	0.70	10.64	0.19	380	0.27	4110	1030
140	0.83	11.22	0.17	274	0.17	1340	243
80	0.97	8.20	0.25	3390	---	---	700

shows the time-dependent carrier temperature ( $T_c$ ) as a function of time. Carrier temperature is extracted by fitting the high energy exponential tail of the GSB feature between  $\sim 1.7$  and 1.9 eV depending on the time zero GSB peak energy (Figure S6) using eq 3,

$$\frac{\Delta T}{T}(E) = -\Delta A \propto \exp \frac{E_F - E}{k_B T_c} \quad (3)$$

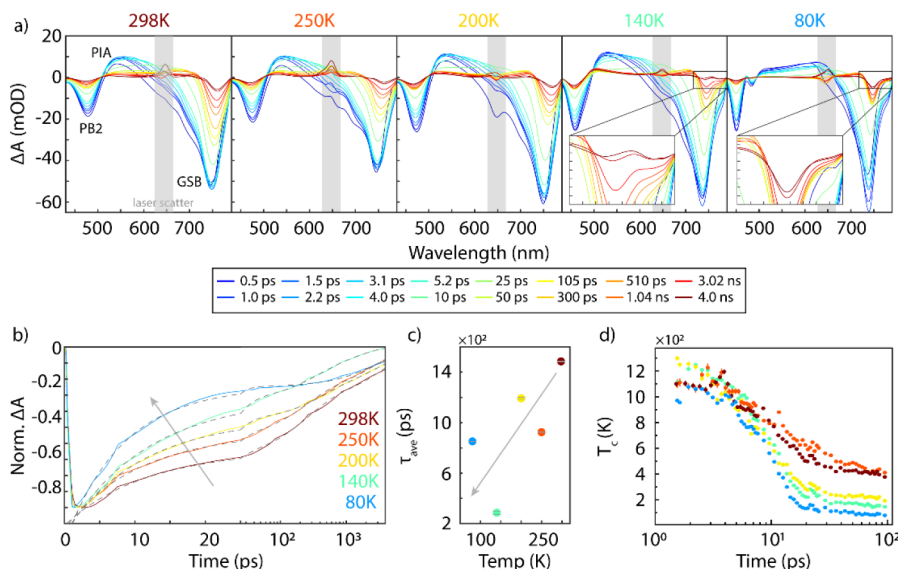


**Figure 6.** (a) Transient absorbance spectra from selected delay times at 298 K, 250 K, 200 K, 140 K, and 80 K for MAFA (30 nm) taken under 650 nm pump ( $4.77 \text{ mJ cm}^{-2}$ ). Characteristic perovskite photobleach (PB2), ground state bleach (GSB), and photoinduced absorption (PIA) are labeled. Excess laser scattering is denoted by gray box. Spectral insets in 140 and 80 K spectra highlight the GSB splitting at later delay times. (b) MAFA GSB kinetics for the various temperatures with multiexponential fits included as dashed gray lines. (c) Calculated GSB average weighted lifetime ( $\tau_{ave}$ ) from each temperature. (d) Extracted carrier temperatures for the MAFA film across the measured temperatures.

where  $E_F$  is the quasi-Fermi level.<sup>54</sup> Here, the TA data are subjected to a fast Fourier transform filtering process with a cutoff frequency of 30 meV<sup>-1</sup> in order to filter out noise and etaloning. The time-dependent dynamics of the carrier temperature are representative of a hot-phonon bottleneck, as carrier-phonon relaxation typically occurs on a faster time scale.<sup>54</sup> As sample temperature decreases, carrier temperature decreases more rapidly within a single phase (250–140 K), where the baseline of carrier temperature at a long time (near ~100 ps) reflects the actual sample temperature. However, both the highest temperature (298 K), where a fraction of the perovskite is still locked in the cubic structure from the annealing process, and the lowest temperature (80 K) slightly differ in their dynamics and maximum carrier temperature. In perovskites, the phase transitions from cubic → tetragonal → orthorhombic are connected to specific soft-phonon modes caused by the tilting of the [PbI<sub>6</sub>]<sup>-</sup> octahedra.<sup>55</sup> Hence, the phonon spectrum of the MAFA perovskite is clearly affected by the phase transitions.

## CONCLUSIONS

In summary, we observe interesting temperature-dependent behavior for the mixed cation MAFA perovskite upon cooling to 20 K. The expected first order phase transition from the tetragonal to the orthorhombic phase is observed at ~110 K. The perovskite bandgap continuously decreases as the phase transition is approached, at which temperature the absorption abruptly red-shifts and two optical transitions are observed. The PL shows the emergence of a third emissive state, one more than observed in previous reports for MAPbI<sub>3</sub>.<sup>27</sup> No signs of degradation are observed in XAS nor TA, indicating that underlying perovskite decomposition and subsequent generation of PbI<sub>2</sub> are not the cause of the observed effects.

In contrast to previous reports on the temperature-dependent behavior of perovskites, our work here introduces another variable into the temperature dependence of perovskites: the mixed A-site cation. We attribute the unique optical properties at low temperature to the formation of methylammonium-richer (MA<sub>0.85+x</sub>FA<sub>0.15-x</sub>PbI<sub>3</sub>) phase and formamidinium-richer (MA<sub>0.85-x</sub>FA<sub>0.15+x</sub>PbI<sub>3</sub>) phases. Overall, the decrease in temperature and subsequent phase transitions results in an increase in PL quantum yield, elongation of the carrier lifetime, changes in the carrier temperatures, and changes in the phonon spectrum, emphasizing the continued promise of perovskites in energy applications.

## ASSOCIATED CONTENT

### Data Availability Statement

The raw data is available at DOI: 10.17605/OSF.IO/FDTXV

### Supporting Information

The Supporting Information is available free of charge at <https://pubs.acs.org/doi/10.1021/acs.chemmater.4c02026>.

Temperature-dependent optical properties of MAPbI<sub>3</sub>, temperature-dependent MAFA absorption and emission spectra showing hysteresis, Gaussian fitting results, temperature-dependent lifetimes and carrier temperature extraction fits (PDF)

## AUTHOR INFORMATION

### Corresponding Author

Lea Nienhaus – Department of Chemistry, Rice University, Houston, Texas 77005, United States; Rice Advanced

Materials Institute, Rice University, Houston, Texas, 77005, United States Department of Physics and Astronomy, Rice University, Houston, Texas 77005, United States;

orcid.org/0000-0003-1412-412X; Email: nienhaus@rice.edu

## Authors

Colette M. Sullivan – Department of Chemistry, Rice University, Houston, Texas 77005, United States; Department of Chemistry and Biochemistry, Florida State University, Tallahassee, Florida 32306, United States;

orcid.org/0000-0001-8660-4056

Jason E. Kuszynski – Department of Chemistry and Biochemistry, Florida State University, Tallahassee, Florida 32306, United States; orcid.org/0000-0002-9458-6940

Alexey Kovalev – National High Magnetic Field Laboratory, Tallahassee, Florida 32310, United States

Nozomi Shirato – Center for Nanoscale Materials, Argonne National Laboratory, Lemont, Illinois 60439, United States

Volker Rose – Advanced Photon Source, Argonne National Laboratory, Lemont, Illinois 60439, United States

Sarah Wiegold – Advanced Photon Source, Argonne National Laboratory, Lemont, Illinois 60439, United States;

orcid.org/0000-0001-6169-3961

Theo Siegrist – National High Magnetic Field Laboratory, Tallahassee, Florida 32310, United States; FAMU-FSU College of Engineering, Tallahassee, Florida 32310, United States; orcid.org/0000-0001-5368-1442

Richard D. Schaller – Center for Nanoscale Materials, Argonne National Laboratory, Lemont, Illinois 60439, United States; orcid.org/0000-0001-9696-8830

Geoffrey F. Strouse – Department of Chemistry and Biochemistry, Florida State University, Tallahassee, Florida 32306, United States; orcid.org/0000-0003-0841-282X

Complete contact information is available at:

<https://pubs.acs.org/10.1021/acs.chemmater.4c02026>

## Author Contributions

<sup>∇</sup>C.M.S. and J.E.K. contributed equally.

## Notes

The authors declare no competing financial interest.

## ACKNOWLEDGMENTS

C.M.S. and L.N. acknowledge funding by the National Science Foundation under Grant No. DMR-2237977 and the Camille and Henry Dreyfus Foundation (TC-23-050). J.E.K. and G.F.S. acknowledge the National Science Foundation under Grant No. DMR-1905757. J.E.K. thanks the Department of Defense for funding from the SMART Scholarship under OUSD/R&E, NDEP/BA-1. A.S. and T.S. performed part of the work at the National High Magnetic Field Laboratory, which is supported by the National Science Foundation under grant DMR-1644779 and the State of Florida. T.S. acknowledges funding by the National Science Foundation under Grant No. DMR-2219906. This work was performed, in part, at the Center for Nanoscale Materials, a U.S. Department of Energy Office of Science User Facility, and the Advanced Photon Source, a U.S. Department of Energy Office of Science User Facility, supported by the U.S. Department of Energy, Office of Science, under Contract No. DE-AC02-06CH11357.

## REFERENCES

- (1) Min, H.; Lee, D. Y.; Kim, J.; Kim, G.; Lee, K. S.; Kim, J.; Paik, M. J.; Kim, Y. K.; Kim, K. S.; Kim, M. G.; Shin, T. J.; Seok, S., II Perovskite Solar Cells with Atomically Coherent Interlayers on SnO<sub>2</sub> Electrodes. *Nature* **2021**, 598 (7881), 444–450.
- (2) Stranks, S. D.; Eperon, G. E.; Grancini, G.; Menelaou, C.; Alcocer, M. J. P.; Leijtens, T.; Herz, L. M.; Petrozza, A.; Snaith, H. J. Electron-Hole Diffusion Lengths Exceeding 1 Micrometer in an Organometal Trihalide Perovskite Absorber. *Science* **2013**, 342 (6156), 341–344.
- (3) Xing, G.; Mathews, N.; Sun, S.; Lim, S. S.; Lam, Y. M.; Grätzel, M.; Mhaisalkar, S.; Sum, T. C. Long-Range Balanced Electron- and Hole-Transport Lengths in Organic-Inorganic CH<sub>3</sub>NH<sub>3</sub>PbI<sub>3</sub>. *Science* **2013**, 342 (6156), 344–347.
- (4) Tress, W.; Marinova, N.; Inganäs, O.; Nazeeruddin, M. K.; Zakeeruddin, S. M.; Graetzel, M. Predicting the Open-Circuit Voltage of CH<sub>3</sub>NH<sub>3</sub>PbI<sub>3</sub> Perovskite Solar Cells Using Electroluminescence and Photovoltaic Quantum Efficiency Spectra: The Role of Radiative and Non-Radiative Recombination. *Adv. Energy Mater.* **2015**, 5 (3), 1400812.
- (5) Bieber, A. S.; VanOrman, Z. A.; Drozdick, H. K.; Weiss, R.; Wieghold, S.; Nienhaus, L. Mixed Halide Bulk Perovskite Triplet Sensitizers: Interplay between Band Alignment, Mid-Gap Traps, and Phonons. *J. Chem. Phys.* **2021**, 155 (23), 234706.
- (6) Tao, S.; Schmidt, I.; Brocks, G.; Jiang, J.; Tranca, I.; Meerholz, K.; Olthof, S. Absolute Energy Level Positions in Tin- and Lead-Based Halide Perovskites. *Nat. Commun.* **2019**, 10 (1), 2560.
- (7) Amat, A.; Mosconi, E.; Ronca, E.; Quarti, C.; Umari, P.; Nazeeruddin, M. K.; Grätzel, M.; De Angelis, F. Cation-Induced Band-Gap Tuning in Organohalide Perovskites: Interplay of Spin–Orbit Coupling and Octahedra Tilting. *Nano Lett.* **2014**, 14 (6), 3608–3616.
- (8) Lee, M. M.; Teuscher, J.; Miyasaka, T.; Murakami, T. N.; Snaith, H. J. Efficient Hybrid Solar Cells Based on Meso-Superstructured Organometal Halide Perovskites. *Science* **2012**, 338 (6107), 643–647.
- (9) Eperon, G. E.; Leijtens, T.; Bush, K. A.; Prasanna, R.; Green, T.; Wang, J. T.-W.; McMeekin, D. P.; Volonakis, G.; Milot, R. L.; May, R.; Palmstrom, A.; Slotcavage, D. J.; Belisle, R. A.; Patel, J. B.; Parrott, E. S.; Sutton, R. J.; Ma, W.; Moghadam, F.; Conings, B.; Babayigit, A.; Boyen, H.-G.; Bent, S.; Giustino, H.; Herz, L. M.; Johnston, M. B.; McGehee, M. D.; Snaith, H. J. Perovskite-Perovskite Tandem Photovoltaics with Optimized Band Gaps. *Science* **2016**, 354 (6314), 861–865.
- (10) Khenkin, M. V.; Katz, E. A.; Abate, A.; Bardizza, G.; Berry, J. J.; Brabec, C.; Brunetti, F.; Bulović, V.; Burlingame, Q.; Di Carlo, A.; et al. Consensus Statement for Stability Assessment and Reporting for Perovskite Photovoltaics Based on ISOS Procedures. *Nat. Energy* **2020**, 5 (1), 35–49.
- (11) Kojima, A.; Teshima, K.; Shirai, Y.; Miyasaka, T. Organometal Halide Perovskites as Visible-Light Sensitizers for Photovoltaic Cells. *J. Am. Chem. Soc.* **2009**, 131 (17), 6050–6051.
- (12) Shao, H.; Wu, X.; Zhou, D.; Chen, W.; Li, L.; Xu, W.; Xu, L.; Dong, B.; Bai, X.; Song, H. Efficient Radiative Enhancement in Perovskite Light-Emitting Devices through Involving a Novel Sandwich Localized Surface Plasmon Structure. *Small Methods* **2022**, 6 (4), 2200163.
- (13) Tan, Z.-K.; Moghaddam, R. S.; Lai, M. L.; Docampo, P.; Higler, R.; Deschler, F.; Price, M.; Sadhanala, A.; Pazos, L. M.; Credgington, D.; Hanusch, F.; Bein, T.; Snaith, H. J.; Friend, R. H. Bright Light-Emitting Diodes Based on Organometal Halide Perovskite. *Nat. Nanotechnol.* **2014**, 9 (9), 687–692.
- (14) Jia, K.; Song, L.; Hu, Y.; Guo, X.; Liu, X.; Geng, C.; Xu, S.; Fan, R.; Huang, L.; Luan, N.; Bi, W. Improved Performance for Thermally Evaporated Perovskite Light-Emitting Devices via Defect Passivation and Carrier Regulation. *ACS Appl. Mater. Interfaces* **2020**, 12 (13), 15928–15933.
- (15) Abdelmageed, G.; Mackeen, C.; Hellier, K.; Jewell, L.; Seymour, L.; Tingwald, M.; Bridges, F.; Zhang, J. Z.; Carter, S. Effect of Temperature on Light Induced Degradation in Methylammonium Lead Iodide Perovskite Thin Films and Solar Cells. *Sol. Energy Mater. Sol. Cells* **2018**, 174, 566–571.
- (16) Wieghold, S.; Bieber, A. S.; Mardani, M.; Siegrist, T.; Nienhaus, L. Understanding the Effect of Light and Temperature on the Optical Properties and Stability of Mixed-Ion Halide Perovskites. *J. Mater. Chem. C* **2020**, 8 (28), 9714–9723.
- (17) Bieber, A. S.; Sullivan, C. M.; Shulenberger, K. E.; Moller, G.; Mardani, M.; Wieghold, S.; Siegrist, T.; Nienhaus, L. Perovskite-Sensitized Upconversion under Operando Conditions. *J. Phys. Chem. C* **2023**, 127 (9), 4773–4783.
- (18) Kieslich, G.; Sun, S.; Cheetham, A. K. Solid-State Principles Applied to Organic–Inorganic Perovskites: New Tricks for an Old Dog. *Chem. Sci.* **2014**, 5 (12), 4712–4715.
- (19) Hemant Kumar, M.; Yantara, N.; Dharani, S.; Graetzel, M.; Mhaisalkar, S.; Boix, P.; Mathews, N. Flexible, Low-Temperature, Solution Processed ZnO-Based Perovskite Solid State Solar Cells. *Chem. Commun.* **2013**, 49 (94), 11089–11091.
- (20) Xin, D.; Wang, Z.; Zhang, M.; Zheng, X.; Qin, Y.; Zhu, J.; Zhang, W.-H. Green Anti-Solvent Processed Efficient Flexible Perovskite Solar Cells. *ACS Sustainable Chem. Eng.* **2019**, 7 (4), 4343–4350.
- (21) Brown, C. R.; Eperon, G. E.; Whiteside, V. R.; Sellers, I. R. Potential of High-Stability Perovskite Solar Cells for Low-Intensity–Low-Temperature (LILT) Outer Planetary Space Missions. *ACS Appl. Energy Mater.* **2019**, 2 (1), 814–821.
- (22) Miyazawa, Y.; Ikegami, M.; Chen, H.-W.; Ohshima, T.; Imazumi, M.; Hirose, K.; Miyasaka, T. Tolerance of Perovskite Solar Cell to High-Energy Particle Irradiations in Space Environment. *iScience* **2018**, 2, 148–155.
- (23) Jacobsson, T. J.; Correa-Baena, J.-P.; Pazoki, M.; Saliba, M.; Schenk, K.; Grätzel, M.; Hagfeldt, A. Exploration of the Compositional Space for Mixed Lead Halogen Perovskites for High Efficiency Solar Cells. *Energy Environ. Sci.* **2016**, 9 (5), 1706–1724.
- (24) Stranks, S. D.; Burlakov, V. M.; Leijtens, T.; Ball, J. M.; Goriely, A.; Snaith, H. J. Recombination Kinetics in Organic-Inorganic Perovskites: Excitons, Free Charge, and Subgap States. *Phys. Rev. Appl.* **2014**, 2 (3), 034007.
- (25) Sullivan, C. M.; Kuszynski, J. E.; Kovalev, A.; Siegrist, T.; Schaller, R. D.; Strouse, G. F.; Nienhaus, L. Cool Carriers: Triplet Diffusion Dominates Upconversion Yield. *Nanoscale* **2023**, 15 (46), 18832–18841.
- (26) Yamada, Y.; Kanemitsu, Y. Electron-Phonon Interactions in Halide Perovskites. *NPG Asia Mater.* **2022**, 14 (1), 1–15.
- (27) Dar, M. I.; Jacopin, G.; Meloni, S.; Mattoni, A.; Arora, N.; Boziki, A.; Zakeeruddin, S. M.; Rothlisberger, U.; Grätzel, M. Origin of Unusual Bandgap Shift and Dual Emission in Organic-Inorganic Lead Halide Perovskites. *Sci. Adv.* **2016**, 2 (10), No. e1601156.
- (28) Shirato, N.; Cummings, M.; Kersell, H.; Li, Y.; Stripe, B.; Rosenmann, D.; Hla, S.-W.; Rose, V. Elemental Fingerprinting of Materials with Sensitivity at the Atomic Limit. *Nano Lett.* **2014**, 14 (11), 6499–6504.
- (29) Rose, V.; Shirato, N.; Bartlein, M.; Deriy, A.; Ajayi, T.; Rosenmann, D.; Hla, S.-W.; Fisher, M.; Reininger, R. XTIP – the World’s First Beamline Dedicated to the Synchrotron X-Ray Scanning Tunneling Microscopy Technique. *J. Synchrotron Radiat.* **2020**, 27 (3), 836–843.
- (30) Xu, J.; Yu, S.; Shang, X.; Chen, X. Temperature Dependence of Bandgap in Lead-Halide Perovskites with Corner-Sharing Octahedra. *Adv. Photonics Res.* **2023**, 4 (1), 2200193.
- (31) Varshni, Y. P. Temperature Dependence of the Energy Gap in Semiconductors. *Physica* **1967**, 34 (1), 149–154.
- (32) Saidi, W. A.; Kachmar, A. Effects of Electron–Phonon Coupling on Electronic Properties of Methylammonium Lead Iodide Perovskites. *J. Phys. Chem. Lett.* **2018**, 9 (24), 7090–7097.
- (33) Jacobsson, T. J.; Schwan, L. J.; Ottosson, M.; Hagfeldt, A.; Edvinsson, T. Determination of Thermal Expansion Coefficients and Locating the Temperature-Induced Phase Transition in Methylammonium Lead Perovskites Using X-Ray Diffraction. *Inorg. Chem.* **2015**, 54 (22), 10678–10685.

- (34) Xing, G.; Mathews, N.; Lim, S. S.; Yantara, N.; Liu, X.; Sabba, D.; Grätzel, M.; Mhaisalkar, S.; Sum, T. C. Low-Temperature Solution-Processed Wavelength-Tunable Perovskites for Lasing. *Nat. Mater.* **2014**, *13* (5), 476–480.
- (35) Fang, H.-H.; Raissa, R.; Abdu-Aguye, M.; Adjokatsse, S.; Blake, G. R.; Even, J.; Loi, M. A. Photophysics of Organic–Inorganic Hybrid Lead Iodide Perovskite Single Crystals. *Adv. Funct. Mater.* **2015**, *25* (16), 2378–2385.
- (36) Kong, W.; Ye, Z.; Qi, Z.; Zhang, B.; Wang, M.; Rahimi-Iman, A.; Wu, H. Characterization of an Abnormal Photoluminescence Behavior upon Crystal-Phase Transition of Perovskite  $\text{CH}_3\text{NH}_3\text{PbI}_3$ . *Phys. Chem. Chem. Phys.* **2015**, *17* (25), 16405–16411.
- (37) Wehrenfennig, C.; Liu, M.; Snaith, H. J.; Johnston, M. B.; Herz, L. M. Charge Carrier Recombination Channels in the Low-Temperature Phase of Organic-Inorganic Lead Halide Perovskite Thin Films. *APL Mater.* **2014**, *2* (8), 081513.
- (38) Panzer, F.; Baderschneider, S.; Gujar, T. P.; Unger, T.; Bagnich, S.; Jakoby, M.; Bässler, H.; Hüttner, S.; Köhler, J.; Moos, R.; Thelakkat, M.; Hildner, R.; Köhler, A. Reversible Laser-Induced Amplified Spontaneous Emission from Coexisting Tetragonal and Orthorhombic Phases in Hybrid Lead Halide Perovskites. *Adv. Opt. Mater.* **2016**, *4* (6), 917–928.
- (39) Wu, K.; Bera, A.; Ma, C.; Du, Y.; Yang, Y.; Li, L.; Wu, T. Temperature-Dependent Excitonic Photoluminescence of Hybrid Organometal Halide Perovskite Films. *Phys. Chem. Chem. Phys.* **2014**, *16* (41), 22476–22481.
- (40) Li, W.; Hao, M.; Baktash, A.; Wang, L.; Etheridge, J. The Role of Ion Migration, Octahedral Tilt, and the A-Site Cation on the Instability of  $\text{Cs}_{1-x}\text{FAxPbI}_3$ . *Nat. Commun.* **2023**, *14* (1), 8523.
- (41) Angel, R. J.; Zhao, J.; Ross, N. L. General Rules for Predicting Phase Transitions in Perovskites Due to Octahedral Tilting. *Phys. Rev. Lett.* **2005**, *95* (2), 025503.
- (42) Ouyang, X.; Chen, W.; Zhang, Y.; Zhang, F.; Zhuang, Y.; Jie, X.; Liu, L.; Wang, D. Structural Phase Transition Involving Octahedron Tilting and Ion Migration in Metal-Halide Perovskites: A Machine-Learning Study. *Phys. Rev. B* **2023**, *108* (2), L020103.
- (43) Bieber, A. S.; VanOrman, Z. A.; Wieghold, S.; Nienhaus, L. Perovskite-Sensitized Upconversion Bingo: Stoichiometry, Composition, Solvent, or Temperature? *J. Chem. Phys.* **2020**, *153* (8), 084703.
- (44) Milot, R. L.; Eperon, G. E.; Snaith, H. J.; Johnston, M. B.; Herz, L. M. Temperature-Dependent Charge-Carrier Dynamics in  $\text{CH}_3\text{NH}_3\text{PbI}_3$  Perovskite Thin Films. *Adv. Funct. Mater.* **2015**, *25* (39), 6218–6227.
- (45) Rudin, S.; Reinecke, T. L.; Segall, B. Temperature-Dependent Exciton Linewidths in Semiconductors. *Phys. Rev. B* **1990**, *42* (17), 11218–11231.
- (46) Wright, A. D.; Verdi, C.; Milot, R. L.; Eperon, G. E.; Pérez-Osorio, M. A.; Snaith, H. J.; Giustino, F.; Johnston, M. B.; Herz, L. M. Electron–Phonon Coupling in Hybrid Lead Halide Perovskites. *Nat. Commun.* **2016**, *7* (1), 11755.
- (47) Wang, H.; Whittaker-Brooks, L.; Fleming, G. R. Exciton and Free Charge Dynamics of Methylammonium Lead Iodide Perovskites Are Different in the Tetragonal and Orthorhombic Phases. *J. Phys. Chem. C* **2015**, *119* (34), 19590–19595.
- (48) Ajayi, T. M.; Shirato, N.; Rojas, T.; Wieghold, S.; Cheng, X.; Latt, K. Z.; Trainer, D. J.; Dandu, N. K.; Li, Y.; Premarathna, S.; Sarkar, S.; Rosenmann, D.; Liu, Y.; Kyritsakas, N.; Wang, S.; Masson, E.; Rose, V.; Li, X.; Ngo, A. T.; Hla, S.-W. Characterization of Just One Atom Using Synchrotron X-Rays. *Nature* **2023**, *618* (7963), 69–73.
- (49) Wieghold, S.; Cope, E. M.; Moller, G.; Shirato, N.; Guzelturk, B.; Rose, V.; Nienhaus, L. Stressing Halide Perovskites with Light and Electric Fields. *ACS Energy Lett.* **2022**, *7* (7), 2211–2218.
- (50) Wieghold, S.; Luo, Y.; Bieber, A. S.; Lackner, J.; Shirato, N.; VanOrman, Z. A.; Rosenmann, D.; Nienhaus, K.; Lai, B.; Nienhaus, G. U.; Rose, V.; Nienhaus, L. Impact of Transition Metal Doping on the Structural and Optical Properties of Halide Perovskites. *Chem. Mater.* **2021**, *33* (15), 6099–6107.
- (51) Wieghold, S.; Shirato, N.; Rose, V.; Nienhaus, L. Investigating the Effect of Electric Fields on Lead Halide Perovskites by Scanning Tunneling Microscopy. *J. Appl. Phys.* **2020**, *128* (12), 125303.
- (52) Drisdell, W. S.; Leppert, L.; Sutter-Fella, C. M.; Liang, Y.; Li, Y.; Ngo, Q. P.; Wan, L. F.; Gul, S.; Kroll, T.; Sokaras, D.; Javey, A.; Yano, J.; Neaton, J. B.; Toma, F. M.; Prendergast, D.; Sharp, I. D. Determining Atomic-Scale Structure and Composition of Organo-Lead Halide Perovskites by Combining High-Resolution X-Ray Absorption Spectroscopy and First-Principles Calculations. *ACS Energy Lett.* **2017**, *2* (5), 1183–1189.
- (53) Stamplecoskie, K. G.; Manser, J. S.; Kamat, P. V. Dual Nature of the Excited State in Organic–Inorganic Lead Halide Perovskites. *Energy Environ. Sci.* **2015**, *8* (1), 208–215.
- (54) Yang, Y.; Ostrowski, D. P.; France, R. M.; Zhu, K.; Van De Lagemaat, J.; Luther, J. M.; Beard, M. C. Observation of a Hot-Phonon Bottleneck in Lead-Iodide Perovskites. *Nat. Photonics* **2016**, *10* (1), 53–59.
- (55) Fransson, E.; Rosander, P.; Eriksson, F.; Rahm, J. M.; Tadano, T.; Erhart, P. Limits of the Phonon Quasi-Particle Picture at the Cubic-to-Tetragonal Phase Transition in Halide Perovskites. *Commun. Phys.* **2023**, *6* (1), 1–7.



CAS BIOFINDER DISCOVERY PLATFORM™

**PRECISION DATA  
FOR FASTER  
DRUG  
DISCOVERY**

CAS BioFinder helps you identify targets, biomarkers, and pathways

**Unlock insights**

**CAS**  
A Division of the  
American Chemical Society